Nanoelectronics and Its New Materials – A NEW ERA OF NANOSCIENCE

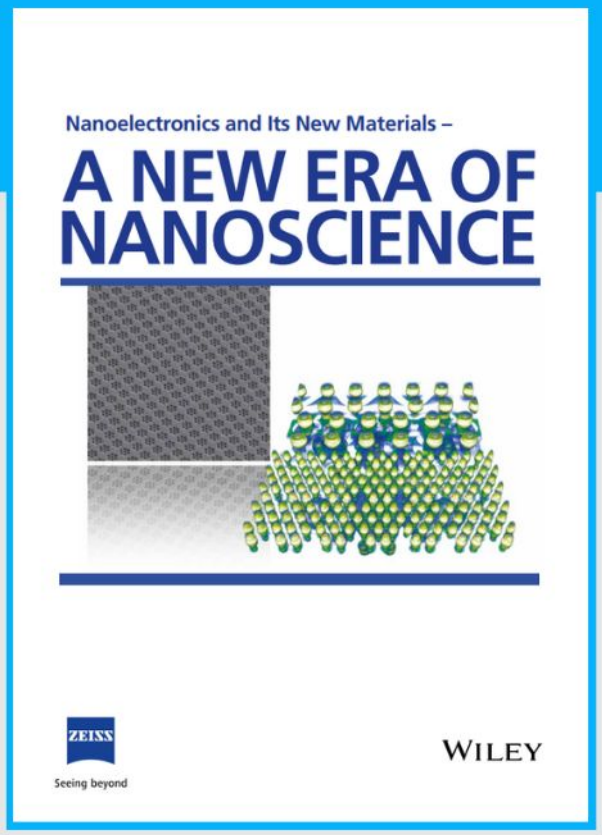

Discover the recent advances in electronics research and fundamental nanoscience.

Nanotechnology has become the driving force behind breakthroughs in engineering, materials science, physics, chemistry, and biological sciences. In this compendium, we delve into a wide range of novel applications that highlight recent advances in electronics research and fundamental nanoscience. From surface analysis and defect detection to tailored optical functionality and transparent nanowire electrodes, this eBook covers key topics that will revolutionize the future of electronics.

To get your hands on this valuable resource and unleash the power of nanotechnology, simply download the eBook now. Stay ahead of the curve and embrace the future of electronics with nanoscience as your guide.

ZEISS

Seeing beyond

WILEY

ADVANCED FUNCTIONAL MATERIALS
www.afm-journal.de

In-Plane Nanowire Growth of Topological Crystalline Insulator $Pb_{1-x}Sn_xTe$

Sander G. Schellingerhout, Roberto Bergamaschini, Marcel A. Verheijen, Francesco Montalenti, Leo Miglio, and Erik P.A.M. Bakkers**

Predicted topological crystalline insulators such as $Pb_{1-x}Sn_xTe$ are an interesting candidate for applications in quantum technology, as they can host spin-polarized surface states. Moreover, in the nanowire geometry, a quasi-1D system can be realized with potential applications exploiting Majorana fermions. Herein, the selective area growth of $Pb_{1-x}Sn_xTe$ islands and nanowires over the full range of x is demonstrated, and their in-depth growth dynamics and faceting are analyzed. By transmission electron microscopy, the single-crystalline and defect-free nature of the grown material and the homogeneous, controllable Pb/Sn ratio in the nanowires is confirmed. With support of phase-field growth simulations, it is shown that the crystal faceting mainly follows the driving force of surface energy minimization, favoring the lowest energy {200} surfaces. A kinetic enhancement of adatom incorporation on {110} facets is recognized to limit their extension with respect to {200} and {111} facets. After inspecting all possible in-plane orientations, we identify the ⟨110⟩ directions as the optimal candidate for the growth of high-quality and perfectly straight $Pb_{1-x}Sn_xTe$ nanowires, enabling the design of complex networks due to their threefold symmetry. This work opens the way to systematic transport investigation of the carrier density in $Pb_{1-x}Sn_xTe$ nanowires and can facilitate further optimization of the $Pb_{1-x}Sn_xTe$ system.

1. Introduction

Tin telluride (SnTe) is predicted to be a Topological crystalline insulator (TCI), a state of matter with spin-polarized surface states arising from crystal symmetries.[1–3] The contribution of the surface states is expected to be more pronounced in nanowires (NWs), due to the high surface to volume ratio,[4,5] and the NW geometry allows for improved coupling to the gate electrodes in devices. However, electronically probing TCI surface states in SnTe is challenging due to the energetically favorable Sn vacancies, which is especially pronounced at Te-rich growth conditions.[6] These vacancies lead to very high carrier densities, and, as a consequence, strong bulk conduction occurs that obscures the topological surface states.[7] In order to reduce the carrier density, a ternary alloy of $Pb_{1-x}Sn_xTe$ can be grown.[8] Although pure PbTe is a trivial (non-topological) material, $Pb_{1-x}Sn_xTe$ is predicted to remain a host of TCI states up to $\approx$ 65% of Pb incorporation.[8–10]

To date, the growth of $Pb_{1-x}Sn_xTe$ NWs has been limited to out-of-plane NWs that suffer from a limited length and are difficult to implement in quantum transport devices.[11–14] In-plane selective area growth (SAG) has some major advantages over the common out-of-plane method, as the thickness of the grown material can be accurately controlled and it allows for straightforward synthesis of complex NW networks such as Hall bar devices for accurate carrier density investigation. Moreover, specific facets can be exposed by choice of the substrate orientation. Of special interest is the {111} family, which is difficult to access for out-of-plane grown NWs, as they are terminated all-around by the lowest surface energy {200} facets.[13] In a sufficiently thin structure, the {111} facets are predicted to host quantum spin Hall (QSH) states.[15,16] Moreover, different facets are expected to host Dirac cones at different positions in the surface Brillouin zone,[17] making it vital to understand and control the growth kinetics and faceting of in-plane SAG $Pb_{1-x}Sn_xTe$.

Here, we investigate the in-plane SAG of the $Pb_{1-x}Sn_xTe$ ternary alloy over the full range of x from 0 to 1, by molecular beam epitaxy (MBE) growth, supported by phase-field simulations. Growth is performed on InP(111)A substrates, as high quality PbTe growth has been shown on this specific substrate

S. G. Schellingerhout, M. A. Verheijen, E. P. Bakkers
Department of Applied Physics
Eindhoven University of Technology
Groene Loper 19, 5612AP Eindhoven, The Netherlands
E-mail: e.p.a.m.bakkers@tue.nl
R. Bergamaschini, F. Montalenti, L. Miglio
L-NESS and Department of Materials Science
University of Milano-Bicocca
via R. Cozzi 55, I-20125 Milano, Italy
E-mail: roberto.bergamaschini@unimib.it
M. A. Verheijen
Eurofins Materials Science Netherlands BV
High Tech Campus 11, 5656AE Eindhoven, The Netherlands

The ORCID identification number(s) for the author(s) of this article can be found under https://doi.org/10.1002/adfm.202305542

DOI: 10.1002/adfm.202305542

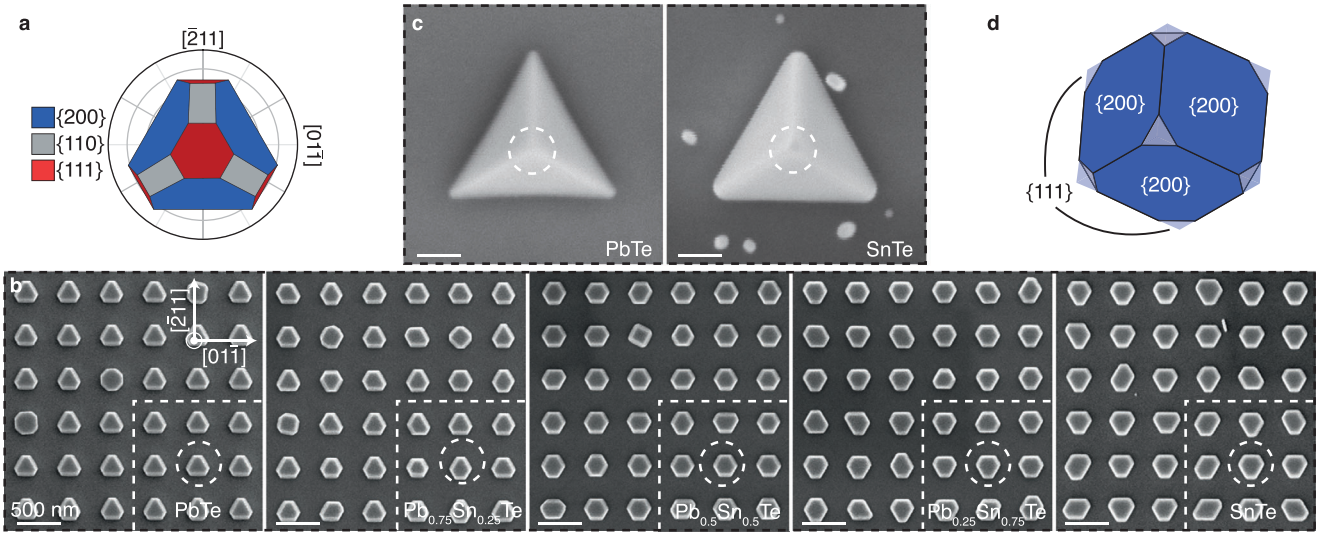

Figure 1. Selective area growth of $Pb_{1-x}Sn_xTe$ alloys in round openings. a) Schematic showing the relevant {200}, {110}, and {111} facets. b) Top-view SEM images showing the SAG of 6 × 6 $Pb_{1-x}Sn_xTe$ structures grown in 200 nm diameter round openings for 30 min. The substrate crystal orientation and scale are indicated in the leftmost panel and are kept consistent throughout. The alloy composition is indicated in each panel. The insets show close-ups, with the mask openings indicated by white circles. c) Top-view SEM images of structures grown in 100 nm openings for 45 min. The morphology for all compositions converges to a tetrahedron terminated by {200} facets. d) Wulff equilibrium shape consisting of only {200} facets (for PbTe) with possible small {111} truncations (light-blue) for SnTe in Te-poor environment.

orientation in previous work,[18] and {111} facets can be readily exposed.

2. Selective Area Growth of $Pb_{1-x}Sn_xTe$

We investigate the SAG of various $Pb_{1-x}Sn_xTe$ compositions. Growth is performed on a semi-insulating InP(111)A substrate, covered with a 20 nm thick amorphous SiN_x mask in which openings are etched to expose the substrate. Details on substrate fabrication are available in Experimental Section.

First, we analyze the growth of $Pb_{1-x}Sn_xTe$ within round openings, focusing on five compositions x evenly distributed over the full range. These allow the grown crystals to develop their preferred morphology when exceeding the mask rims, without any bias by the in-plane directions. In **Figure 1**a, the relevant available facets, consisting of the {200}, {110}, and {111} families, are indicated. Figure 1b shows scanning electron microscopy (SEM) images of the resulting crystals grown in 200 nm diameter openings after 30 min of growth for different $Pb_{1-x}Sn_xTe$ compositions. A representative overview of a 6 × 6 array gives an indication for the high yield and fairly good uniformity of the grown crystals, although a small fraction of deviating crystals can be identified. For all compositions, the resulting morphology consists of a {111} top facet and a combination of inclined {200} and {111} facets. The ratio of dimensions of the {200} and the {111} side facets is distinctly different for the diverse compositions, with an increasing extension of the {111} over the {200} for increasing Sn content. Interestingly, no {110} facets are observed, despite their energy should be comparable to the one of {111} surfaces.[19,20] From the consistent morphology of each crystal with respect to each other, we can conclude that all the crystals, regardless of the composition, have a fixed (epitaxial) relationship to the substrate.

By continuing the deposition for longer times and/or considering smaller opening sizes, shapes from all compositions are found to converge to a tetrahedron defined only by {200} facets, as shown in Figure 1c for PbTe (see also Ref. [18]), and for SnTe islands, grown in 100 nm openings for 45 min. This latter shape, to be considered as the final, steady-growth morphology, looks consistent with the equilibrium morphology (Figure 1d), as predicted on the basis of ab-initio surface energy values for both PbTe[19] and SnTe[20] in a Te-poor environment. This is assumed to be the case in our experiments, as Te is supposed to re-evaporate immediately due to its high vapor pressure.

Next, we investigate the growth of $Pb_{1-x}Sn_xTe$ in elongated openings. **Figure 2**a shows a SEM image of 4 µm long $Pb_{0.5}Sn_{0.5}Te$ NWs, with the orientation of their long axis to the substrate varied in 5° increments. The high-symmetry ⟨110⟩ and ⟨112⟩ directions are identified as the most promising ones. Structures grown along the ⟨110⟩ directions are the most uniform displaying well-defined facets, and therefore we primarily focus on these. The NWs grown along the ⟨112⟩ directions show smaller uniform segments. In Figure 2b,c, NWs grown in a cross pattern in these two crystal directions are shown for x = 0, 0.5, and 1, for different growth times. When the grown structures do not exceed the mask in height (Figure 2b), the morphology of the NWs is identical, and only a flat {111} top facet is visible. When the growth exceeds the mask (Figure 2c), a combination of well-defined facets is formed. For PbTe, a uniform NW growth appears to occur in both the ⟨110⟩ and ⟨112⟩ directions, although a local refaceting occurs at the ends of the ⟨112⟩ oriented NWs that expose the lowest-energy {200} surfaces at one terminal and {111} at the opposite. With increasing Sn content, NWs grown along the in-plane ⟨112⟩ direction form increasingly prominent zigzag-like faceting, probably consisting of alternating {200} and {111} side-facets, in place of {110}

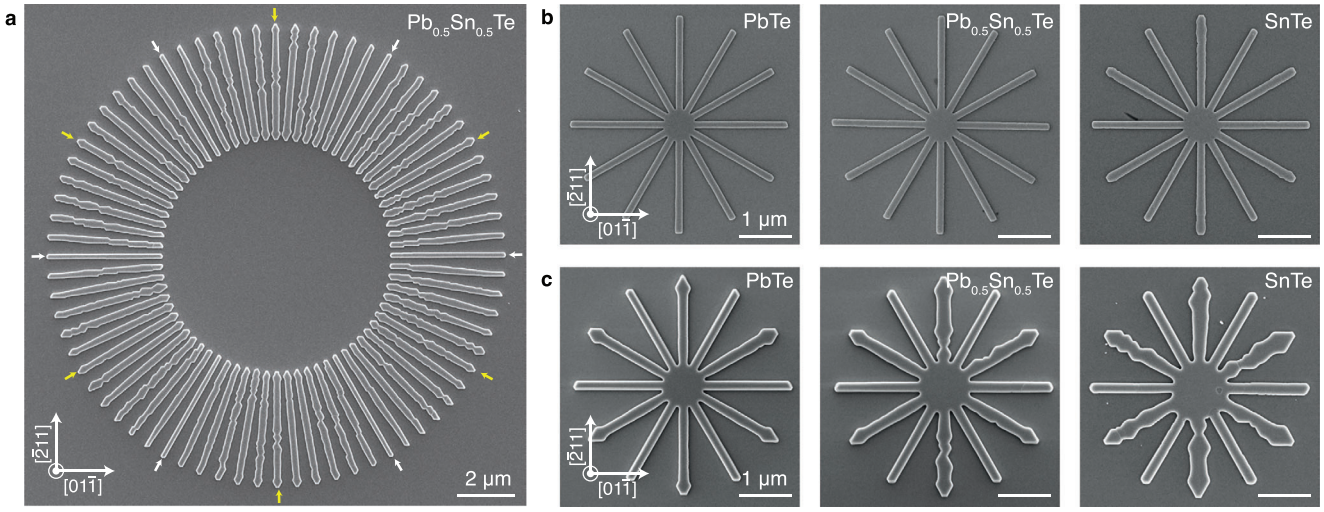

Figure 2. Selective area growth of $Pb_{1-x}Sn_xTe$ alloys as nanowires and networks. a) $Pb_{0.5}Sn_{0.5}Te$ NWs grown for 30 min in 4 μm long openings, their orientation to the substrate rotated at 5° increments. NWs grown in the ⟨110⟩ direction (white arrows) are uniform along their full length, while NWs grown in the ⟨110⟩ direction (yellow arrows) have small uniform segments. b) $Pb_{1-x}Sn_xTe$ NWs grown for 15 min in the ⟨110⟩ and ⟨112⟩ direction at x=0, 0.5, and 1. The networks have barely exceeded the mask, with no distinct faceting visible other than the {111} top facet. c) $Pb_{1-x}Sn_xTe$ NWs grown for 30 min for x=0, 0.5, and 1. The networks exceed the mask and form well defined facets. PbTe appears to form uniform, straight facets in both the ⟨110⟩ and the ⟨112⟩ directions. For increasing Sn content, the ⟨110⟩ oriented nanowires have flat facets, but the ⟨112⟩-oriented wires develop zigzag-like faceting.

vertical facets. High-resolution transmission electron microscopy (HRTEM) analysis of a PbTe NW grown along the in-plane ⟨112⟩ direction, shown in Figure S3 (Supporting Information), indicates that for PbTe the side facets are not flat {110} facets. Actually, these sidewalls display a rounded shape, possibly indicating the same instability of the {110} facets that drives the zigzag formation in Sn alloys. As a consequence of such facet instability in the in-plane ⟨112⟩ direction, we have prioritized the in-plane ⟨110⟩ direction, as for quantum transport experiments a consistent confinement energy is crucial. Due to the threefold symmetry of the ⟨110⟩ direction on the (111)A substrate, complex structures can be grown using a combination of the three available in-plane ⟨110⟩ directions.

3. Material Analysis

Experimentally achieving the TCI phase is dependent on the high purity and the low disorder of the material.[21] The crystalline quality of the PbSnTe system is comparable, for the whole compositional range, to what we have reported for the pure PbTe (on InP) system in Ref. [22]. Also in the PbSnTe system i) growth is initiated with many nuclei with different crystal orientations (111), (111)-twinned, and (100), as observed by SEM imaging; ii) the lattice mismatch between substrate and epilayer is accommodated by misfit dislocations at the InP/PbSnTe interface as evidenced by TEM studies; iii) after merging of the nuclei, large (111)-twinned-oriented PbSnTe crystals are formed, as evidenced from cross-sectional TEM studies. HRTEM and high-angle annular dark field scanning transmission electron microscopy (HAADF-STEM) are performed on cross sections of NWs grown in the [01-1] direction in order to characterize the crystalline quality and faceting of the $Pb_{1-x}Sn_xTe$ NWs. As the $Pb_{0.5}Sn_{0.5}Te$ composition is expected to have a reasonable carrier density, while still being a TCI, the analysis presented here is performed for this composition. **Figure 3**a shows a HAADF-STEM image of a cross section of an array of ten parallel $Pb_{0.5}Sn_{0.5}Te$ NWs, grown and imaged in the in-plane [01-1] direction. Figure 3b shows a HRTEM cross section image of the rightmost NW, revealing the faceting that consists of a {200} side facet on the right side, a {111} side, and top facet and a transition region where a small {110} facet accompanies in a round profile the transition between both {111} facets. An electron diffraction (ED) pattern taken on the same NW and part of the underlying substrate is shown in Figure 3c. The crystal structure of the grown material is identified as the rock-salt crystal structure, and shows an epitaxial, still twinned, relation to the InP substrate. Next, a HAADF-STEM image taken from a similar crystal shows the near-atomically flat $InP/Pb_{0.5}Sn_{0.5}Te$ interface (Figure 3d). From a filtered inverse fast Fourier transformation (iFFT), the atomic rows leading to and from the interface become visible in Figure 3e. We can identify quasi-periodic misfit dislocations, indicated by the red circle, that relieve most of the strain induced by the 8.8% lattice mismatch between the $Pb_{0.5}Sn_{0.5}Te$ NW and the substrate. Next, to confirm the crystal quality along the length of a full NW, ED is performed along the cross section of a 2 × 2 μm crystal shown in Figure 3f, with three ED examples shown in Figure 3g. The structure is single-crystalline over the entire length, with contrast lines visible in the HRTEM due to small-angle mosaicity.[18] For different x-values, the same crystalline quality is found (see Figure S4, Supporting Information).

As the carrier density and the topological properties in the grown material are strongly dependent on the group-IV incorporation, it is vital to have a controllable, uniform Sn-to-Pb ratio in the crystal.[8] To verify the uniformity of the group-IV incorporation in the $Pb_{1-x}Sn_xTe$ NWs, energy dispersive X-ray spectroscopy (EDX) analysis is used, as reported in **Figure 4**. The

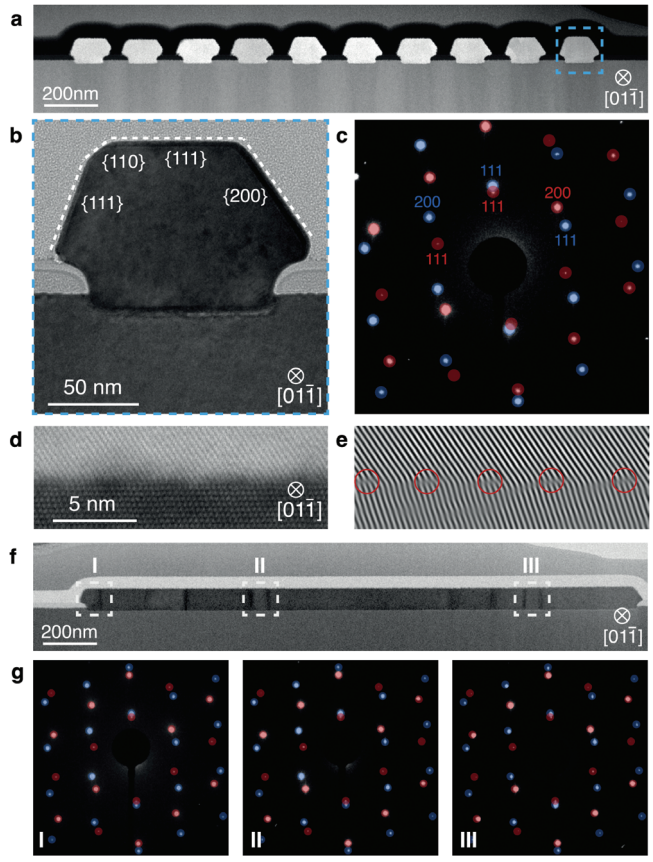

Figure 3. a) Overview HAADF-STEM cross section of an array of ten [01-1] oriented $Pb_{0.5}Sn_{0.5}Te$ NWs grown for 30 min. b) TEM image of the right-most NW in (a). The top and side facets are indicated. c) An electron diffraction pattern taken along the [01-1] zone axis of the same NW, confirming the single-crystalline nature. Diffraction spots originating from $Pb_{0.5}Sn_{0.5}Te$ (red) and InP (blue) are indicated. d) HAADF-STEM at the InP/PbTe interface, showing the near-atomically flat interface. e) Filtered iFFT showing the atomic columns near the InP/PbTe interface, with misfit dislocations (red circles) that relieve most of the lattice mismatch and strain. f) Overview bright-field TEM cross section of a 2 × 2 µm nanostructure. g) ED patterns taken at the points indicated in (f).

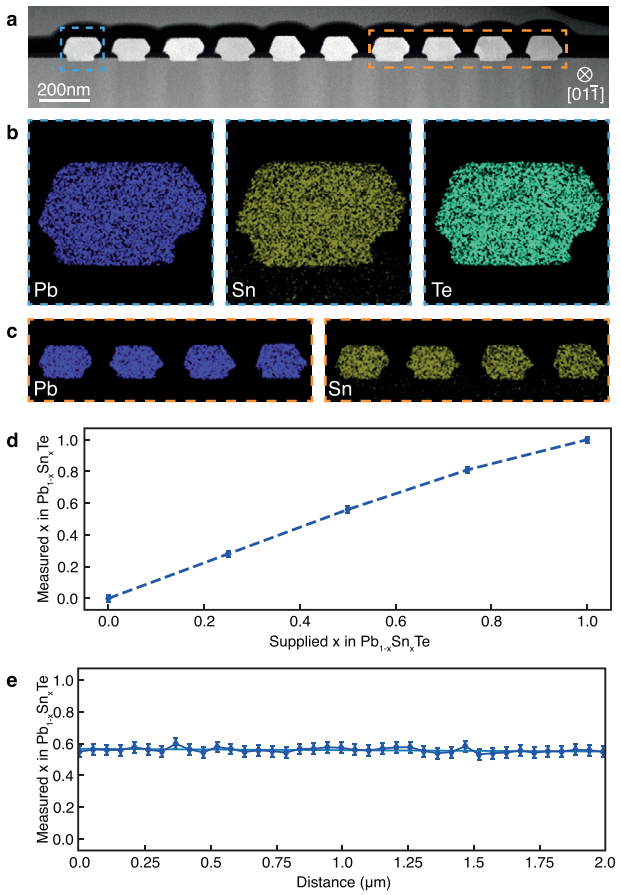

Figure 4. a) Overview HAADF-STEM cross section of an array of ten [01-1] grown $Pb_{0.5}Sn_{0.5}Te$ NWs. b) EDX data showing uniform Pb and Sn incorporation in a NW. c) EDX data showing uniform Pb and Sn incorporation in the adjacent NWs as indicated in (a). d) Measured Sn incorporation as a function of the supplied composition *x*. e) Measured Sn incorporation along a 2 × 2 µm nanostructure, showing uniform incorporation along the full length.

EDX analysis on a single $Pb_{0.5}Sn_{0.5}Te$ NW is shown in Figure 4b, where a sharp interface between the substrate and NW is visible. Moreover, a uniform distribution of Pb and Sn is visible in the NW cross section, indicating that group-IV incorporation during growth is homogeneous. The elemental composition, the dimensions, and the morphology of all the NWs in the array (Figure 4c) are uniform, indicating that there is no competition for material or cross-talk between adjacent structures.[23,24] From this observation, it is likely that growth is mainly driven by direct impingement of material, rather than adatom diffusion over the mask surface. In Figure 4d, we identify a near-linear trend between the Sn fraction of the supplied material and that in the grown structure as obtained from EDX. The EDX analyses of the other *x*-values are available in Figure S5 (Supporting Information). The compositional uniformity along the entire cross section of a 2 × 2 µm structure has been verified by EDX, and is shown in Figure 4e, showing the constant group-IV ratio along the entire structure.

4. Growth Model

Understanding and controlling the morphology at the different growth stages of $Pb_{1-x}Sn_xTe$ crystals are keys for exploring the surface-dependent TCI properties. While a qualitative connection has been recognized between the crystal morphologies in the latest stages of deposition and the faceting of the equilibrium crystal shape (ECS), the actual kinetic pathway driving the morphological evolution at the intermediate stages can only be understood by modeling the growth dynamics. To this purpose, we devise a phase-field model, described in Experimental Section. We trace the advancing of the growth front from within the mask openings as due to deposition and surface diffusion over the NW profile, under the effect of the different facet stabilities and, eventually, adatom incorporation kinetics.

Figure 5a reports the evolution of the growth front for a cross section of a NW grown along the ⟨110⟩ direction, taking as the only driving force the different surface energy of the facets, set according to the ab-initio data.[19] Starting from a flat profile as the initial stage after the pristine filling of the opening bottom,

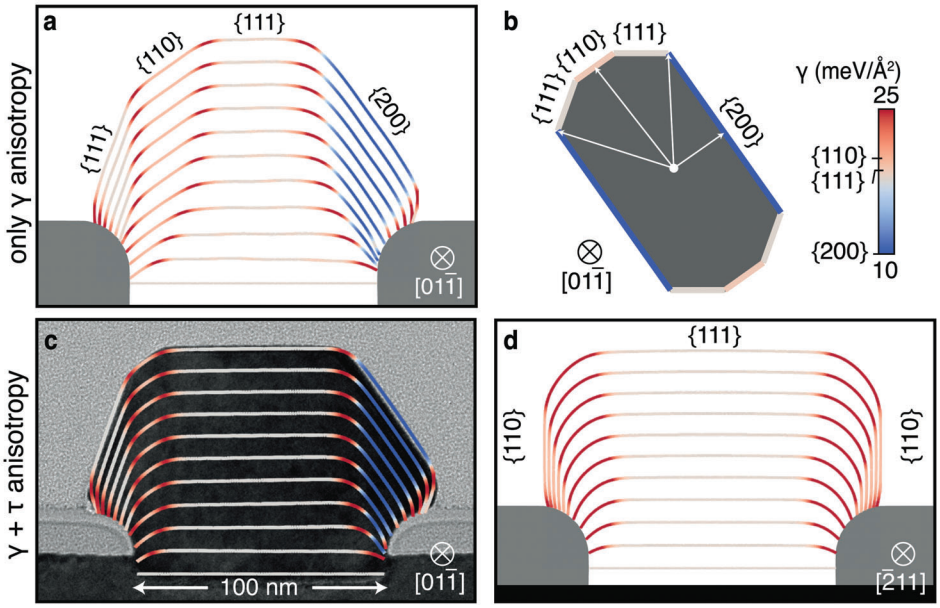

Figure 5. a) Phase-field simulation of the crystal growth for the axial cross-section of a NW along the ⟨110⟩ direction. MBE-like deposition and anisotropic surface energy based on ab-initio data[19] are considered. Profiles correspond to the $\varphi = 0.5$ contour lines taken at regular time intervals, from the initial flat profile (bottom) to the final profile corresponding to 30 min growth. The gray area corresponds to the mask region, modeled via a second phase-field. b) Equilibrium crystal shape for a free-standing NW with ⟨110⟩ axis obtained by the Wulff construction using the same surface energy values of (a). c) Evolution sequence as in (a) but including anisotropic incorporation times τ enhancing the relative growth rate of {110} facets. The TEM cross-section of Figure 3b is reported in the background to show the good correspondence with the simulation. d) Simulation of the profile evolution during the growth of a NW along the ⟨112⟩ direction by the same parameters of panel (c).

the shape evolves toward a higher aspect-ratio as to expose the most convenient {200} facet on one side and a combination of {111} and {110} facets on the other. In particular, in the early stages, a large {110} side facet is formed that later reduces in size as the steeper {111} side appears. In the latest stages, the growth tends to proceed almost self-similarly with {110} and {111} facets having similar sizes as expected because of their comparable surface energy. This indeed looks similar to the upper part of the two-dimensional (2D) equilibrium crystal shape of ⟨110⟩ cross-section of a free-standing PbTe NW depicted in Figure 5b.

In contrast, the typical experimental cross section (see Figure 3b; Figure S4, Supporting Information) clearly shows a much larger {111} flat top and only a very small {110} side facet. Furthermore, we already noticed that {110} facets are never observed during the growth of islands. Given that the ab-initio study in Ref. [19] accurately considered the typical surface reconstructions of the {111} surface as well as the effect of using different energy functionals, still concordant in predicting a wide {110} facet in the 2D ECS, we conclude that the suppression of the {110} facet should be more likely due to an additional kinetic contribution, which enhances the actual growth rate of {110} surfaces and progressively reduces their lateral expansion. We then admit in the model an additional term accounting for the anisotropy of adatom kinetics and impose that incorporation is slower on {200} and {111} facets with respect to {110} (and any other intermediate) orientation. For a best-fitting of the experimental profile of Figure 3b, we find the following incorporation times: $\tau_{200} = \tau_{111} = 10\tau_{110}$.

The evolution sequence obtained by adding incorporation anisotropy to the case of Figure 5a is reported in Figure 5c. In particular, the model now predicts a much wider {111} flat top and only minor {110} side facet compared to the thermodynamic faceting. This results from the additional material flow from the former to the latter facet due to the uneven adatom incorporation. The substantial match with the superimposed TEM image of Figure 3b highlights the efficacy of the kinetic model in providing a realistic evolution pathway, from the pristine flat profile, after filling the opening bottom, to the faceted shape of the overgrown NW.

Taking the model of Figure 5d as validated, using the same parameter set we can then inspect the faceting behavior for the NWs oriented along the ⟨112⟩ direction. In this geometry, only the {111} top facet and two vertical {110} side facets are available parallel to the NW axis. The resulting profile tends to be nearly rectangular except for large rounded regions on the sidewalls, induced by the outward inclination imposed by the non-wetting contact angle on the mask and by the continuous flow of material from the slow-growing {111} top to the fast-growing {110} fronts. This shape looks similar to some TEM cross-sectional views, such as the one reported in Figure S3 (Supporting Information). However, it must be pointed out that the {110} side facets are unstable against break-up into alternating {200} (lowest energy) and {111} surfaces as recognized in the zigzag profiles in Figure 2.

5. Conclusion

We have studied the growth dynamics, facet formation, and Sn-to-Pb ratio incorporation of in-plane $Pb_{1-x}Sn_xTe$ SAG nanowires on InP(111)A substrates. The developed growth scheme allows the synthesis of reproducible, well-defined NWs, and complex NW networks. By using a (111) substrate, the {111} facet of the

grown material is subsequently exposed, and its extension can be controlled with the deposition time and mask opening diameter, according to the evolution predicted by the phase-field simulations. The optimal in-plane growth direction is identified as the threefold symmetric ⟨110⟩ direction, as this forms flat side facets, while NWs grown in the in-plane ⟨112⟩ direction are roughened by zigzag facetting at the sidewalls. The Sn-to-Pb ratio in the grown NWs can be accurately controlled, and it is homogeneous in the entire NW. From the phase-field model, the observed faceting is understood to be driven by surface energy minimization and a kinetic component that shrinks the faster-growing {110} facets in favor of the {111} facets. A substantial overlap is achieved between growth simulation and experiment. Together, these results establish in-plane SAG as a promising material platform for further investigation of the TCI properties of $Pb_{1-x}Sn_xTe$. Preliminary transport experiments show that the carrier densities in our PbSnTe SAG structures are similar to what has been reported before for PbSnTe layers.[8]

6. Experimental Section

Substrate Fabrication: Electron-beam lithography (EBL) markers were etched into undoped semi-insulating (111)A InP substrates by reactive-ion etching using CHF_3 with added O_2.[25] Subsequently, 20 nm SiN_x was deposited by plasma-enhanced chemical vapor deposition. AR-P 6200.13 resist was spun at 4000 rpm on the chip, and baked at 150°C for 60 s. The mask openings were written by EBL and developed in AR 600-546 for 60 s. Reactive ion etching transferred the pattern into the mask. A phosphoric acid wet etch (H_2O:H_3PO_4 = 10:1) removed the native substrate oxides, after which the substrates were loaded into the MBE and degassed at 300°C for 1 h.

$Pb_{1-x}Sn_xTe$ Heteroepitaxy: Growth took place in an ultra-high vacuum MBE system. An annealing step under Te overpressure at 480°C was used for surface reconstruction of the etched openings and to remove oxide residuals from the exposed substrate surface. The $Pb_{1-x}Sn_xTe$ networks were subsequently grown at 340°C with separate elemental sources, providing a Te flux of about 4.00×10^{-7} mbar and a total group-IV flux of about 1.25×10^{-7} mbar measured as beam equivalent pressure using a naked Bayard–Alpert ion gauge. Temperatures were measured with a kSA BandiT system based on the optical absorption edge.

TEM Studies: TEM studies were performed using a probe-corrected JEOL ARM 200F operated at 200 kV, equipped with a 100 mm^2 Centurio SDD Energy dispersive X-ray spectroscopy detector. Misfit dislocations at the InP-$Pb_{0.5}Sn_{0.5}Te$ interface were visualized by first computing the FFT of an atomic resolution image, then applying a filter to only include one InP (111) and the adjacent PbTe (200) spot, and then taking the iFFT of the result.

Phase-Field Model: The phase-field growth model detailed in Ref. [26] was adapted to provide a realistic description of the SAG process[27] (full details are provided in Section S6, Supporting Information). In particular, the evolution of the crystal morphology was traced implicitly by the phase field φ,[28] evolving in time because of the combined effect of material deposition and diffusion along the crystal growth front: $\frac{\partial \varphi}{\partial t} = \Phi(\hat{\mathbf{n}})|\nabla\varphi| + \nabla \cdot [M(\varphi)\nabla\mu]$. Close-to-equilibrium conditions were assumed considering that deposition was slow compared to the surface diffusion (here $\Phi/M \approx 10^{-3}$) such to return the faceted growth via redistribution of the supplied material according to the local gradients of chemical potential μ. A flux distribution $\Phi(\hat{\mathbf{n}})$ reproducing a rotating MBE beam, inclined at 30° from the substrate normal, as in the experimental apparatus, was set. Diffusion was restricted at the surface (i.e., within the φ diffuse-interface) by using a degenerate mobility $M(\varphi) \tilde{} \varphi^2(1-\varphi^2)$ and two main contributions were considered as driving forces. The first was thermodynamic and accounted for the surface energy anisotropy. A strong anisotropy regime was considered by introducing a corner energy regularization term in the form of a Willmore energy[28,29]. More precisely, the implementation proposed in Ref. [30] was followed and the minima for γ were set according to the ab-initio values reported in literature for PbTe in Ref. [19], as obtained by generalized gradient approximation, that is, γ_{200}=10 , γ_{111}=17.5 , and γ_{110}=19 meV Å^{-2} and a baseline energy γ_0=25 meV Å^{-2} (Figure S6b, Supporting Information). Given the similar hierarchy of SnTe surface energies under Te-poor conditions,[20] the values above were assumed to provide a sufficient approximation for all $Pb_{1-x}Sn_xTe$ compositions.

The second contribution to the chemical potential accounted for the orientation-dependent incorporation kinetics and was set proportional to the local velocity $\partial\varphi/\partial t$ itself by a factor τ playing the role of an incorporation time.[26,31] Here, both the case of purely thermodynamic regime with $\tau = 0$ and the case of anisotropic τ were considered. In this latter, the three facet families were taken as maxima of τ with respect to a baseline τ_0, with a slower incorporation on {200} and {111} surfaces, that is, $\tau_{200} = \tau_{111} = 10\tau_{110} = 20\tau_0$ (Figure S6b, Supporting Information).

In order to account for the constraint imposed by the mask opening in SAG, a second order parameter ψ was introduced to trace the mask geometry as the one of experiments. The growth dynamics were confined in the free-space region on top of the mask by using the smoothed boundary method detailed in Ref. [32] (see also Section S6, Supporting Information, Ref. [33]), including an average non-wetting contact angle of 120° estimated from TEM cross-sectional views.

The numerical solution of the time-dependent partial differential equation problem was performed by finite element method via the AMDiS[34,35] toolbox, exploiting a semi-implicit time-integration scheme and adaptive mesh refinement. For the sake of simplicity, only 2D simulations were here considered representative of the axial cross-section of infinitely long NWs. A 500 × 500 nm^2 simulation domain was set, using an interface width ϵ=5 nm for both φ and ψ and mesh resolution of 0.7 nm.

Supporting Information

Supporting Information is available from the Wiley Online Library or from the author.

Acknowledgements

This work was supported by the European Research Council (ERC TOCINA 834290). The authors acknowledge Solliance, a solar energy R & D initiative of ECN, TNO, Holst, TU/e, imec and Forschungszentrum Jülich, and the Dutch province of Noord-Brabant for funding the TEM facility.

Conflict of Interest

The authors declare no conflict of interest.

Data Availability Statement

The data that support the findings of this study are openly available in Zenodo at https://doi.org/10.5281/zenodo.7932634, reference number 7932634.

Keywords

nanowires, PbSnTe, selective area growth, topological insulators

Received: May 18, 2023
Revised: July 20, 2023
Published online:

[1] Y. Tanaka, Z. Ren, T. Sato, K. Nakayama, S. Souma, T. Takahashi, K. Segawa, Y. Ando, *Nat. Phys.* **2012**, *8*, 800.
[2] T. H. Hsieh, H. Lin, J. Liu, W. Duan, A. Bansil, L. Fu, *Nat. Commun.* **2012**, *3*, 982.
[3] N. M. Nguyen, W. Brzezicki, T. Hyart, *Phys. Rev. B* **2022**, *105*, 075310.
[4] D. Kong, J. C. Randel, H. Peng, J. J. Cha, S. Meister, K. Lai, Y. Chen, Z.-X. Shen, H. C. Manoharan, Y. Cui, *Nano Lett.* **2010**, *10*, 329.
[5] F. Xiu, L. He, Y. Wang, L. Cheng, L.-T. Chang, M. Lang, G. Huang, X. Kou, Y. Zhou, X. Jiang, Z. Chen, J. Zou, A. Shailos, K. L. Wang, *Nat. Nanotechnol.* **2011**, *6*, 216.
[6] N. Wang, D. West, J. Liu, J. Li, Q. Yan, B.-L. Gu, S. B. Zhang, W. Duan, *Phys. Rev. B* **2014**, *89*, 045142.
[7] P. B. Littlewood, B. Mihaila, R. K. Schulze, D. J. Safarik, J. E. Gubernatis, A. Bostwick, E. Rotenberg, C. P. Opeil, T. Durakiewicz, J. L. Smith, J. C. Lashley, *Phys. Rev. Lett.* **2010**, *105*, 086404.
[8] V. V. Volobuev, P. S. Mandal, M. Galicka, O. Caha, J. Sánchez-Barriga, D. Di Sante, A. Varykhalov, A. Khiar, S. Picozzi, G. Bauer, P. Kacman, R. Buczko, O. Rader, G. Springholz, *Adv. Mater.* **2017**, *29*, 1604185.
[9] S. O. Ferreira, E. Abramof, P. Motisuke, P. H. O. Rappl, H. Closs, A. Y. Ueta, C. Boschetti, I. N. Bandeira, *J. Appl. Phys.* **1999**, *86*, 7198.
[10] S.-Y. Xu, C. Liu, N. Alidoust, M. Neupane, D. Qian, I. Belopolski, J. Denlinger, Y. Wang, H. Lin, L. Wray, G. Landolt, B. Slomski, J. Dil, A. Marcinkova, E. Morosan, Q. Gibson, R. Sankar, F. Chou, R. Cava, A. Bansil, M. Hasan, *Nat. Commun.* **2012**, *3*, 1192.
[11] Z. Li, S. Shao, N. Li, K. McCall, J. Wang, S. X. Zhang, *Nano Lett.* **2013**, *13*, 5443.
[12] J. Shen, Y. Jung, A. S. Disa, F. J. Walker, C. H. Ahn, J. J. Cha, *Nano Lett.* **2014**, *14*, 4183.
[13] M. Safdar, Q. Wang, Z. Wang, X. Zhan, K. Xu, F. Wang, M. Mirza, J. He, *Nano Lett.* **2015**, *15*, 2485.
[14] P. Liu, H. J. Han, J. Wei, D. Hynek, J. L. Hart, M. G. Han, C. J. Trimble, J. Williams, Y. Zhu, J. J. Cha, *ACS Appl. Electron. Mater.* **2021**, *3*, 184.
[15] J. Liu, L. Fu, *Phys. Rev. B* **2015**, *91*, 081407.
[16] S. Safaei, M. Galicka, P. Kacman, R. Buczko, *New J. Phys.* **2015**, *17*, 063041.
[17] Y. Tanaka, T. Shoman, K. Nakayama, S. Souma, T. Sato, T. Takahashi, M. Novak, K. Segawa, Y. Ando, *Phys. Rev. B* **2013**, *88*, 235126.
[18] J. Jung, S. G. Schellingerhout, M. F. Ritter, S. C. ten Kate, O. A. van der Molen, S. de Loijer, M. A. Verheijen, H. Riel, F. Nichele, E. P. Bakkers, *Adv. Funct. Mater.* **2022**, *32*, 2208974.
[19] V. L. Deringer, R. Dronskowski, *J. Phys. Chem. C* **2013**, *117*, 24455.
[20] V. L. Deringer, R. Dronskowski, *ChemPhysChem* **2013**, *14*, 3108.
[21] J. Moore, *Nat. Phys.* **2009**, *5*, 378.
[22] J. Jung, S. G. Schellingerhout, O. A. H. van der Molen, W. H. J. Peeters, M. A. Verheijen, E. P. A. M. Bakkers, *Phys. Rev. Mater.* **2023**, *7*, 023401.
[23] M. T. Borgström, G. Immink, B. Ketelaars, R. Algra, E. P. Bakkers, *Nat. Nanotechnol.* **2007**, *2*, 541.
[24] M. E. Cachaza, A. W. Christensen, D. Beznasyuk, T. Særkjær, M. H. Madsen, R. Tanta, G. Nagda, S. Schuwalow, P. Krogstrup, *Phys. Rev. Mater.* **2021**, *5*, 094601.
[25] H. Jung, D.-Y. Park, F. Xiao, K. H. Lee, Y.-H. Choa, B. Yoo, N. V. Myung, *J. Phys. Chem. C* **2011**, *115*, 2993.
[26] M. Albani, R. Bergamaschini, M. Salvalaglio, A. Voigt, L. Miglio, F. Montalenti, *Phys. Status Solidi B* **2019**, *256*, 1800518.
[27] M. Albani, L. Ghisalberti, R. Bergamaschini, M. Friedl, M. Salvalaglio, A. Voigt, F. Montalenti, G. Tütüncüoglu, A. Fontcuberta i Morral, L. Miglio, *Phys. Rev. Mater.* **2018**, *2*, 093404.
[28] B. Li, J. Lowengrub, A. Rätz, A. Voigt, *Commun. Comput. Phys.* **2009**, *6*, 433.
[29] S. Torabi, J. Lowengrub, A. Voigt, S. Wise, *Proc. R. Soc. A* **2009**, *465*, 1337.
[30] M. Salvalaglio, R. Backofen, R. Bergamaschini, F. Montalenti, A. Voigt, *Cryst. Growth Des.* **2015**, *15*, 2787.
[31] J. W. Cahn, J. E. Taylor, *Acta Metall. Mater.* **1994**, *42*, 1045.
[32] H.-C. Yu, H.-Y. Chen, K. Thornton, *Model. Simul. Mater. Sci. Eng.* **2012**, *20*, 075008.
[33] L. K. Aagesen, M. E. Coltrin, J. Han, K. Thornton, *J. Appl. Phys.* **2015**, *117*, 194302.
[34] S. Vey, A. Voigt, *Comput. Vis. Sci.* **2007**, *10*, 57.
[35] T. Witkowski, S. Ling, S. Praetorius, A. Voigt, *Adv. Comput. Math.* **2015**, *41*, 1145.